JPE 18-5-11

https://doi.org/10.6113/JPE.2018.18.5.1409
ISSN(Print): 1598-2092 / ISSN(Online): 2093-4718

SynRM Servo-Drive CVT Systems Using MRRHPNN Control with Mend ACO

Jung-Chu Ting† and Der-Fa Chen*

†,*Dept. of Industrial Education and Technology, National Changhua University of Education, Changhua, Taiwan

Abstract

Compared with classical linear controllers, a nonlinear controller can result in better control performance for the nonlinear uncertainties of continuously variable transmission (CVT) systems that are driven by a synchronous reluctance motor (SynRM). Improved control performance can be seen in the nonlinear uncertainties behavior of CVT systems by using the proposed mingled revised recurrent Hermite polynomial neural network (MRRHPNN) control with mend ant colony optimization (ACO). The MRRHPNN control with mend ACO can carry out the overlooker control system, reformed recurrent Hermite polynomial neural network (RRHPNN) control with an adaptive law, and reimbursed control with an appraised law. Additionally, in accordance with the Lyapunov stability theorem, the adaptive law in the RRHPNN and the appraised law of the reimbursed control are established. Furthermore, to help improve convergence and to obtain better learning performance, the mend ACO is utilized for adjusting the two varied learning rates of the two parameters in the RRHPNN. Finally, comparative examples are illustrated by experimental results to confirm that the proposed control system can achieve better control performance.

Key words: Ant colony optimization, Continuously variable transmission, Lyapunov stability, Recurrent Hermite polynomial neural network, Synchronous reluctance motor

I. INTRODUCTION

Compared with other motors, the synchronous reluctance motor (SynRM) through optimal design methods [1], [2] is one of highest efficiency and lowest cost. A lot of work [3]-[6] has been dedicated to the drive and control of the SynRM due to advancements in terms of optimal design methods and power electronics technologies. However, SynRM servo-drive continuously variable transmission (CVT) systems [7], [8] have not been proposed in the study of dynamic control. The CVT speed control has been reported in many papers [9], [10]. The dynamic responses of a CVT system are studied in this paper.

Owing to the inherent parallel structure and good learning ability [11], [12] of neural networks, they have better approximation capability in modeling nonlinear systems. Thus, they have computationally expensive trainings that take a large number of iterations to complete. To bring down the computational complexity, a functional-type neural network (NN) [13]-[16] with a much lower computational cost has been introduced. The functional-type NN has less computational complexity and a faster convergence than a conventional NN in the performance execution phase. Ma et al. [17], [18] proposed a computationally efficient Hermite polynomial NN. Constructing Hermite polynomial expansions were adopted by using the structure and function level adaptation methodologies. This Hermite polynomial NN can effectively catch the underlying input-output map. Rigatos et al. [19] proposed a Hermite polynomial NN that can be used in nonparametric estimation. Siniscalchi et al. [20] proposed a Hermite polynomial NN for application in connectionist speech recognition systems with speaker adaptation. However, these Hermite polynomial NNs were most applied for system modelling and image processing. Moreover, the weight updates of these NNs did not utilize the internal information of the NNs and they were sensitive to function approximation in the training procedure. Owing to increased precision approximation in modelling nonlinear systems and dynamic control [13]-[16], many researchers have been fascinated with recurrent neural network (RNN) studies. These RNNs are

Manuscript received Oct. 15, 2017; accepted May 11, 2018
Recommended for publication by Associate Editor Dong-Hee Lee.
†Corresponding Author: d0331019@gm.ncue.edu.tw
Tel: +886-47232105-7205, Fax: +886-47211287, National Changhua University of Education
*Dept. Ind. Education & Tech., Nat'l Changhua Univ. Education, Taiwan

able to carry out the identification and control of complex dynamics system. However, they have higher computational costs. The proposed reformed recurrent Hermite polynomial neural network (RRHPNN) has better dynamic mapping performance and less computational time in the presence of uncertainties. In this study, the proposed mingled reformed recurrent Hermite polynomial neural network (MRRHPNN) control system with mend ACO for controlling SynRM servo-drive CVT systems with nonlinear dynamics is presented in order to reduce computational complexity and raise system robustness.

Due to the highly nonlinear dynamics of V-belt CVT systems many controllers do not provide satisfactory control performance. Thus, the MRRHPNN control system, which is composed of the overlooker control, RRHPNN control with an adaptive law, and reimbursed control with an appraised law, is applied to CVT systems driven by a SynRM. However, the fixed learning rates of the parameters and the varied learning rates of the parameters may not be the globally optimal learning rates of weight parameters. Therefore, in order to assure the globally optimal learning rates of the weight parameters, the mend ACO is employed to adjust the two varied learning rates of the weight parameters in the RRHPNN. The MRRHPNN control using the mend ACO has fast learning ability and good generalization capability in the presence of the lumped nonlinear disturbances. The adaptive law of the online parameters in the RRHPNN can be derived according to the Lyapunov stability theorem and the gradient descent method. Furthermore, mend ACO is employed to adjust the two varied learning rates of the weight parameters in the RRHPNN in order to achieve better convergence. Finally, the control performances of the proposed MRRHPNN control using mend ACO are verified by experimental results.

This paper is organized as follows. Section II presents the structure of the SynRM servo-drive CVT system. Section III presents the design method of the MRRHPNN control system with mend ACO. Section IV presents a number of experimental results. Section V provides some conclusions.

II. Structure of a SynRM Servo-Drive CVT System

The geometric constitution for the simplified kinematics of a CVT system with negligible belt flexural effects and slip losses is illustrated in Fig. 1. The torque dynamic equations [7]-[10] shown in Fig. 1(a) and Fig. 1(b) with the front driving shaft and the rear driven shaft using the law of conservation can be simplified as:

$$T_e = J_a\dot{\omega}_r + B_a\omega_r + T_1 \tag{1}$$

$$T_2 = J_2\dot{\omega}_2 + B_2\omega_2 + T_2^l(v_{a2},\tau_{a2},F_{2l},B_2,\omega_2^2) \tag{2}$$

where $T_1 = T_1^l(T_a,\Delta T,F_l(B_2),\upsilon_a(v_2,B_2),\tau_a(v_2),\omega_r^2) + J_1\dot{\omega}_r + B_1\omega_r$ is

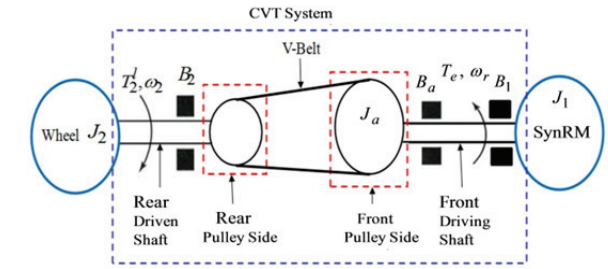

(a)

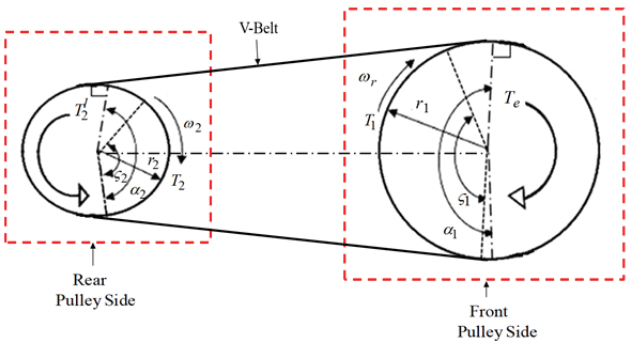

(b)

Fig. 1. Geometric constitution of a CVT system driven by a SynRM: (a) Sketch graph of the SynRM-wheel set via the CVT connection, (b) Geometric graph of the CVT system.

the equivalent driven torque at the front pulley shaft. $\sigma_2 = \sigma_2(\varsigma_1,\varsigma_2)$ is the conversion ratio between the front pulley shaft and the rear pulley shaft. $(\varsigma_1,\varsigma_2)$ is the sliding active arcs to contribute torque transmission at a low speed. (α_1,α_2) are the wrap angles of the belt-pulley contacting arcs. T_2 is the driven torque of the rear pulley shaft. $T_2^l(v_{a2},\tau_{a2},F_{2l},B_2,\omega_2^2)$ is the lumped nonlinear external disturbances including the rolling resistance v_{a2}, the wind resistance τ_{a2} and the braking force F_{2l}. In addition, J_2, B_2, J_a and B_a are the mechanical angular velocity of the rotor representing the moment of inertia of the wheel, the viscous friction coefficients of the wheel, the moment of inertia of the front pulley side, and the viscous friction coefficients of the front pulley side, respectively. ω_2 and ω_r are the speed of the rear pulley shaft and the mechanical angular speed of the rotor, respectively. Then the torque equation can be transformed from the rear pulley side to the front pulley side by using the speed ratio and the sliding ratio [7]-[10]. It is assumed that the belt flexural effects, the power and the slip losses are neglected.

Consequently, the combined dynamic equations [7-10] of the SynRM servo-drive CVT system from (1) to (2) can be presented by:

$$T_e = T_1^l(T_a,\Delta T,F_l(B_2),\upsilon_a(v_2,B_2),\tau_a(v_2),\omega_r^2) + J_r\dot{\omega}_r + B_r\omega_r \tag{3}$$

where $T_1^l(T_a,\Delta T,F_l(B_2),\upsilon_a(v_2,B_2),\tau_a(v_2),\omega_r^2) = T_a + \Delta T + T_u$ [7]-[10]

is the combined lumped nonlinear external disturbances and parameter variations. T_a, $\Delta T = \Delta J_r \dot{\omega}_r + \Delta B_r \omega_r$ and $T_u = F_l(B_2) + \upsilon_a(v_2, B_2) + \tau_a(v_2)\omega_r^2$ are the fixed load torque, the combined parameter variation and the combined unknown nonlinear load torque, respectively. $\upsilon_a(v_2, B_2)$, $\tau_a(v_2)$ and $F_l(B_2)$ are the combined rolling resistance, the combined wind resistance and the combined braking force, respectively. $B_r = B_1 + B_a$ and $J_r = J_1 + J_a$ are the combined viscous friction coefficient and the combined moment of inertia, respectively. J_1 and B_1 represent the moment of inertia of the SynRM and the viscous friction coefficients of the SynRM, respectively. Detailed specifications of the tested vehicle include the conversion ratio $\sigma_2 = 1.77$, the pulley radius $(r_1 = 13.2\ cm, r_2 = 9.6\ cm)$, the wrap angles of the belt-pulley contacting arcs $(\alpha_1 = 165\ Degree, \alpha_2 = 135\ Degree)$, the sliding active arcs to contribute torque transmission at low speeds $(\varsigma_1 = 125\ Degree, \varsigma_2 = 105\ Degree)$, the wheel tire 100/90-10, the V-Belt length $L_1 = 67.6\ cm$, $J_a = 0.82 \times 10^{-3}\ Nms^2$, $J_2 = 2.16 \times 10^{-3}\ Nms^2$, $B_a = 1.12 \times 10^{-3}\ Nms/rad$ and $B_2 = 4.36 \times 10^{-3}\ Nms/rad$.

The synchronously rotating reference frame of the SynRM with the *d*-*q* axis frame can be offered as [3]-[6]:

$$u_Q = r_s\, i_Q + L_Q\, \dot{i}_Q + p_n \omega_r L_D\, i_D / 2 \tag{4}$$

$$u_D = r_s\, i_D + L_D\, \dot{i}_D - p_n \omega_r L_Q\, i_Q / 2 \tag{5}$$

where u_D, i_D and L_D are the *d*-axis stator voltage, current and inductance, respectively. u_Q, i_Q and L_Q are the *q*-axis stator voltage, current and inductance, respectively. r_s is the stator resistance. p_n is the number of poles. The electromagnetic torque can be denoted as:

$$T_e = 3 p_n \left[\left(L_D - L_Q\right) i_Q i_D\right] / 4 \tag{6}$$

The motor dynamics equation is:

$$T_e = T_l + B_1 \omega_r + J_1 \dot{\omega}_r \tag{7}$$

where T_e stands for the electromagnetic torque, and $T_l = T_1^l(T_a, \Delta T, F_l(B_2), \upsilon_a(v_2, B_2), \tau_a(v_2), \omega_r^2) + J_a \dot{\omega}_r + B_a \omega_r$ stands the load torque. A sketch graph of a SynRM servo-drive CVT system is shown in Fig. 2.

The entire system of a SynRM servo-drive CVT can be denoted as: a speed/torque control system, a field-oriented control, interlock and isolated circuits, voltage source inverter (VSI) with three-sets of insulated-gate bipolar transistor (IGBT) power modules, a SynRM servo-drive system and a CVT system. The field-oriented control consists of a sinusoidal pulse width modulation (PWM) control modulator, a proportional-integral (PI) current control, a coordinate translation system including inverse coordinate translation, $\sin\theta_f / \cos\theta_f$ generation and lookup table generation. A

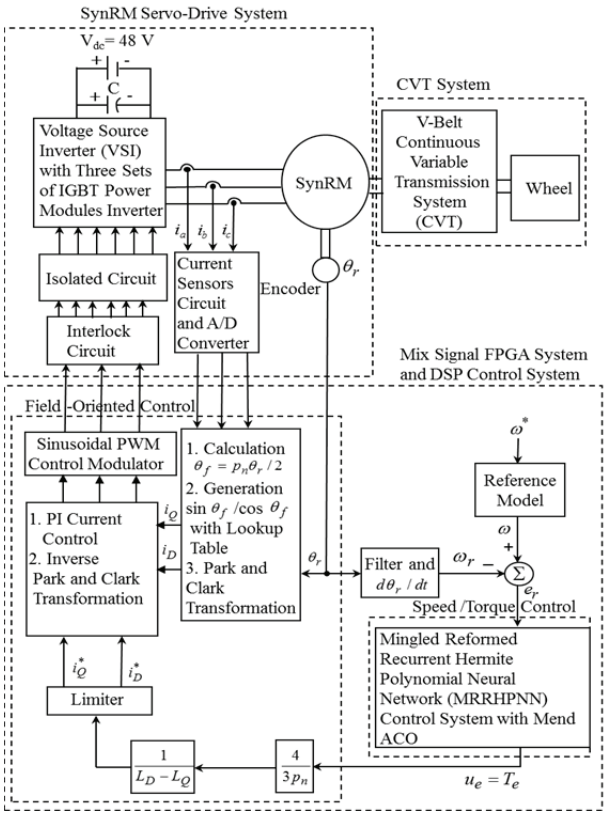

Fig. 2. Sketch graph of a SynRM servo-drive CVT system.

mix signal field-programmable-gate-array (FPGA) system using a Xilinx Spartan-XCS05XL-4VQ100I-ND chip with 80 Mhz, 3,200 distributed RAM bits, 5,000 gates and 77 input/output (I/O) ports was used to achieve field-oriented control. A digital-signal-processor (DSP) control system using a Texas Instrument (TI) TMS320F28335 chip with 150 Mhz, 256K × 16 Flash RAM, 34K × 16 SARAM, 16 sets of channels analog-digital converters (ADC) with 12-bits, 18 sets of programmable-PWM ports, 6 sets of high-resolution PWM ports and 2 sets of quadrature encoder interfaces was used to achieve speed/torque control.

Two gains for the PI current controller are given as follows: $k_{ic} = k_{pc} / T_{ic} = 6.22$ and $k_{pc} = 12.5$ through some heuristic knowledge [26]-[28] to obtain a better dynamic response. The specifications of the SynRM are the three-phase, two-pole, 48 V, 1.5 kW and 3600 *rpm*. The electrical/mechanical parameters of the SynRM are given as: $r_s = 0.88\ \Omega$, $L_Q = 22.15\ mH$, $L_D = 146.68\ mH$, $J_1 = 1.02 \times 10^{-3}\ Nms^2$ and $B_1 = 3.28 \times 10^{-3}\ Nms / rad$. The SynRM servo-drive CVT system was operated under lumped external disturbances and nonlinear uncertainties.

III. MRRHPNN Control with Mend ACO

For simplifying the MRRHPNN control system with a mend ACO design, the dynamic model from (3) can be

represented as:

$$\dot{\omega}_r = T_e / J_r - T_1^l(T_a, \Delta T, F_l(B_2), \upsilon_a(v_2, B_2), \tau_a(v_2), \omega_r^2)/J_r - B_r\omega_r / J_r$$
$$= A_e u_e + B_e T_1^l(T_a, \Delta T, F_l(B_2), \upsilon_a(v_2, B_2), \tau_a(v_2), \omega_r^2)/J_r + C_e\omega_r \quad (8)$$

where $A_e = 1/J_r$, $B_e = -1/J_r$ and $C_e = -B_r/J_r$ are three known constants. $u_e = T_e$ is the control effort, i.e., the command torque of the SynRM. When uncertainties arise, the parameters can be assumed to be bounded, i.e., $|C_e\omega_r| \le D_3(\omega_r)$, $\left|B_e T_1^l(T_a, \Delta T, F_l(B_2), \upsilon_a(v_2, B_2), \tau_a(v_2), \omega_r^2)\right| \le D_2$ and $D_1 \le A_e$. In addition, $D_3(\omega_r)$ is a known continuous function. D_1 and D_2 are two known constants. The tracked error can hereafter be defined as:

$$e_r = \omega - \omega_r \quad (9)$$

where e_r is the difference between the desired speed ω and the rotor speed ω_r. Then the consummate control law under uncertain perturbations for the SynRM servo-drive CVT system can be designed as:

$$u_e^* = [\dot{\omega} + k_e e_r - C_e\omega_r - B_e T_1^l(T_a, \Delta T, F_l(B_2), \upsilon_a(v_2, B_2), \tau_a(v_2), \omega_r^2)]/A_e \quad (10)$$

where k_e is a positive constant. Equation (8) using (9) and (10) with $u_e^* = u_e$ can be rewritten as:

$$\dot{e}_r + k_e e_r = 0 \quad (11)$$

When $e_r(t) \to 0$ as $t \to \infty$ in (11). Then the rotor speed asymptotically tracks the desired value. For reducing the tracked error, the MRRHPNN control system with mend ACO, shown in Fig. 3, was proposed for controlling the SynRM servo-drive CVT system under uncertain perturbations. The proposed MRRHPNN control system with mend ACO is made up of an overlooker control, a RRPHNN control with an adaptive law, and a reimbursed control with an appraised law. The control law can be designed as:

$$u_e = u_1 + u_2 + u_3 \quad (12)$$

where u_1, u_2 and u_3 are the overlooker control system, the RRHPNN controller and the reimbursed controller, respectively. The overlooker control system can stabilized the states of the controlled system around a predetermined bound area. The RRHPNN controller was acted as the major tracking controller to imitate a consummate control law. The reimbursed controller can reimburse the difference between the consummate control law and the RRHPNN controller.

The MRRHPNN control system with mend ACO can be uniformly close to the consummate control law to extend the divergent state back inside the predestinated bound region. Hereafter, the stability of the MRRHPNN control system with mend ACO can be guaranteed. Equation (8) using (9), (10), (11) and (12) can be rewritten as:

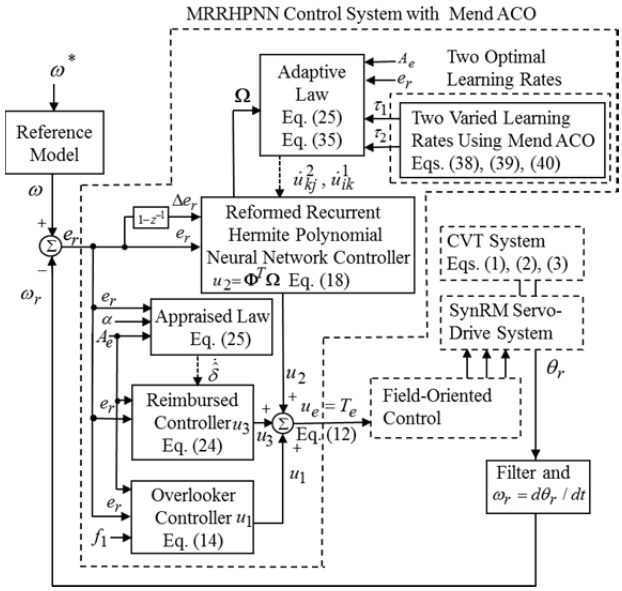

Fig. 3. Constitution of the MRRHPNN control system with mend ACO.

$$\dot{e}_r = -k_e e_r + [u_e^* - u_1 - u_2 - u_3]A_e \quad (13)$$

Firstly, the overlooker control u_1 can be designed as:

$$u_1 = f_1 \,\mathrm{sgn}(e_r A_e)[D_3(\omega_r) + D_2 + |\dot{\omega}| + |k_e e_r|]/A_e \quad (14)$$

where $\mathrm{sgn}(\cdot)$ is a sign function. The overseer control law on $f_1 = 1$ is valid when the RRHPNN affinity properties cannot be guaranteed. The overlooker control emerges in overdone effort due to an insufficient bound, e.g., D_1, D_2, $D_3(\omega_r)$ and the sign function. Therefore, the RRHPNN control and the reimbursed control can be designed to conquer the overdone effort. The RRHPNN control was advanced to imitate the consummate control. Then the reimbursed control was evolved to reimburse the difference between the consummate control and the RRHPNN control.

Secondly, the construction of the proposed three-layer RRPHNN with input, hidden and output layers is shown in Fig. 4. The transmitted signals of the RRPHNN are listed in the following stages.

(1) The input and output signals in the input layer at node *i* are denoted as:

$$o_i^1 = l_i^1(\prod_k a_i^1(N) u_{ik}^1 \, o_k^3(N-1)), \quad i = 1, 2 \quad (15)$$

where l_i^1 is an activation function using a linear function, and Π is the multiplier, which multiplies all of the input signals. In addition, $a_1^1 = e_r = (\omega - \omega_r)$ is the error, $a_2^1 = e_r(1 - z^{-1}) = \Delta e_r$ is the error variation, u_{ik}^1 is the recurrent weight from the output layer to the input layer; o_k^3 is the output in the output layer, and N is the number of iterations.

(2) The input and output signals in the hidden layer at node *j* are denoted as:

$$o_j^2 = H_j(\sum_{i=1}^{2} o_i^1(N) + \varepsilon\, o_j^2(N-1)),\ j = 0, 1, \cdots, m-1 \tag{16}$$

where H_j is the Hermite polynomial [29]-[32] which is the activation function in the hidden layer. $\sum$ is the summation, which summates all of the input signals. In addition, ε is the self-feedback gain of the hidden layer which is between 0 and 1, o_i^1 is the output in the input layer, o_j^2 is the output in the hidden layer, and *m* is the number of nodes. The Hermite polynomials [29]-[32] $H_n(x)$ are the arguments of polynomials with $-1 < x < 1$, where *n* is the order of expansion. The zero, first and second order Hermite polynomials are given by $H_0(x) = 1$, $H_1(x) = 2x$ and $H_2(x) = 4x^2 - 2$, respectively. Higher-order Hermite polynomials emerge through the recursive method $H_{n+1}(x) = 2xH_n(x) - 2nH_{n-1}(x)$.

(3) The input and output signals in the output layer at node *k* are expressed as:

$$o_k^3 = l_k^3(\sum_{j=0}^{m-1} u_{kj}^2\, o_j^2(N)),\quad k = 1 \tag{17}$$

where l_k^3 is the activation function using a linear function, $\sum$ is the summation, which summates all of the input signals. In addition, u_{kj}^2 is the connective weight between the hidden layer and the output layer. $a_j^3(N) = o_j^2(N)$ is the *j*th input signal of the output layer. The output of the output layer can be presented as $o_k^3(N) = u_2$. Thus, the output of the RRPHNN can be expressed as:

$$u_2 = \mathbf{\Phi}^T \mathbf{\Omega} \tag{18}$$

where $\mathbf{\Phi} = \begin{bmatrix} u_{10}^2 & \cdots & u_{1(m-1)}^2 \end{bmatrix}^T$ is the weight vector of the connective weights between the hidden layer and the output layer, $\mathbf{\Omega} = \begin{bmatrix} a_0^3 & \cdots & a_{(m-1)}^3 \end{bmatrix}^T$ is the input vector in the output layer, and a_j^3 is the Hermite polynomials.

Thirdly, to execute the reimbursed control u_3, a minimum congenial error φ can be presented as:

$$\varphi = u_e^* - u_2^* = u_e^* - (\mathbf{\Phi}^*)^T \mathbf{\Omega} \tag{19}$$

where $|\varphi| < \rho$, ρ is a very small positive value, and $\mathbf{\Phi}^*$ is the consummate weight vector to achieve the minimum congenial error. Equation (13) using (19) can be denoted as:

$$\begin{aligned} \dot{e}_r &= -k_e e_r + [u_e^* - u_1 - u_2 - u_3] A_e \\ &= -k_e e_r + [(u_e^* - u_2^*) + (u_2^* - u_2) - u_3 - u_1] A_e \\ &= -k_e e_r + [(u_e^* - (\mathbf{\Phi}^*)^T) + ((\mathbf{\Phi}^*)^T - (\mathbf{\Phi})^T)\mathbf{\Omega} - u_3 - u_1] A_e \\ &= -k_e e_r + [\varphi + (\mathbf{\Phi}^* - \mathbf{\Phi})^T)\mathbf{\Omega} - u_3 - u_1] A_e \end{aligned} \tag{20}$$

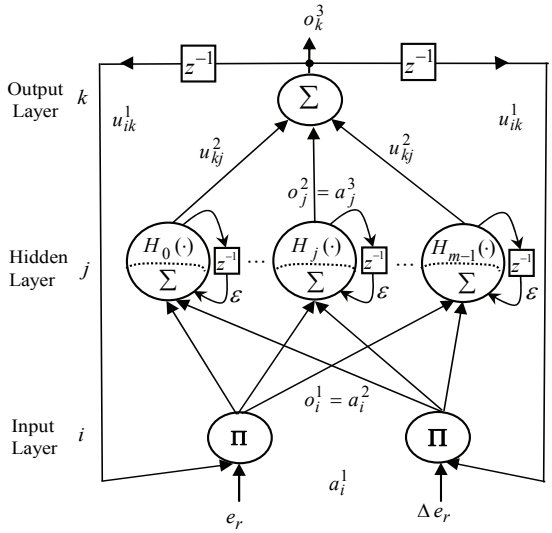

Fig. 4. Construction of the three-layer RRHPNN.

Moreover, the following Lyapunov function was chosen:

$$P(t) = e_r^2/2 + [(\mathbf{\Phi}^* - \mathbf{\Phi})^T(\mathbf{\Phi}^* - \mathbf{\Phi})/(2\tau_1) + \tilde{\delta}^2/(2\alpha) \tag{21}$$

where τ_1 is the learning rate, $\tilde{\delta} = \hat{\delta} - \delta$ is the appraised error, and α is the adaptive gain. Using (19) and (20), and then differentiating (21) yields:

$$\begin{aligned} \dot{P}(t) &= e_r\, \dot{e}_r - (\mathbf{\Phi}^* - \mathbf{\Phi})^T \dot{\mathbf{\Phi}}/\tau_1 + \tilde{\delta}\dot{\hat{\delta}}/\alpha \\ &= -k_e e_r^2 + [\varphi + (\mathbf{\Phi}^* - \mathbf{\Phi})^T \mathbf{\Omega} - u_3 - u_1] e_r A_e - (\mathbf{\Phi}^* - \mathbf{\Phi})^T \dot{\mathbf{\Phi}}/\tau_1 \\ &\quad + \tilde{\delta}\dot{\hat{\delta}}/\alpha \end{aligned} \tag{22}$$

For achieving $\dot{P}(t) \le 0$, the adaptive law $\dot{\mathbf{\Phi}}$, the reimbursed controller u_3, and the appraised law $\dot{\hat{\delta}}$ can be designed as:

$$\dot{\mathbf{\Phi}} = \tau_1 \mathbf{\Omega}\, e_r\, A_e \tag{23}$$

$$u_3 = \hat{\delta}\,\mathrm{sgn}(e_r A_e) \tag{24}$$

$$\dot{\hat{\delta}} = \alpha |e_r A_e| \tag{25}$$

If (14), (19) and (24) are substituted into (22), and if (14) with $f_1 = 1$ is used, (22) can be denoted as:

$$\dot{P}(t) = -k_e e_r^2 + (\varphi - \hat{\delta}\,\mathrm{sgn}(e_r A_e)) e_r A_e + \tilde{\delta}\dot{\hat{\delta}}/\alpha \tag{26}$$

Equation (26) using (25) can be denoted as:

$$\dot{P}(t) \le -k_e e_r^2 + (\varphi - \delta)|e_r A_e| \le -k_e e_r^2 \le 0 \tag{27}$$

Equation (27) shows $\dot{P}_1(t)$ to be negative semi-definite, i.e., $P(t) \le P(0)$. This implies that e_r and $(\mathbf{\Phi}^* - \mathbf{\Phi})$ are bounded. Additionally, the function is defined as:

$$Q_1(t) = -\dot{P}(t) = k_e e_r^2 \tag{28}$$

The integration of (27) gives:

$$\int_0^t Q_1(\varsigma)d\varsigma = \int_0^t -[P(\varsigma)]d\varsigma = P(0) - P(t) \tag{29}$$

Because $P(t)$ is a non-increasing and bounded, while $P(0)$ is bounded:

$$\lim_{t\to\infty} \int_0^t Q_1(\varsigma)\, d\varsigma < \infty \tag{30}$$

Differentiating (28) gives:

$$\dot{Q}_1(t) = 2k_e e_r \dot{e}_r \tag{31}$$

By using Barbalat's lemma [33], [34], $\dot{e}_r$ is also bounded. $Q_1(t)$ is a uniformly continuous function [33], [34], and $\lim_{t\to\infty} Q_1(t) = 0$ when all of the variables on the right-hand side of (20) are bounded. Therefore, $e_r(t) \to 0$ as $t \to \infty$. Moreover, $\mathrm{sgn}(e_r A_e)$ can be replaced by the equation $(e_r A_e)/(|e_r A_e| + \kappa)$ to avoid the chattering phenomenon of reimbursed controller u_3 with a positive constant κ.

The adaptive law $\dot{\Phi}$ in the RRHPNN with online parameters training can be computed using the Lyapunov stability theorem and the gradient descent method. Moreover, two optimal learning rates are used for the training parameters of the RRHPNN to accomplish better convergence of error. The adaptive law $\dot{\Phi}$ shown in (23) can be represented as:

$$\dot{u}_{kj}^2 = \tau_1 o_j^2 e_r A_e \tag{32}$$

Then, the cost function is defined as [13]:

$$P_1 = e_r^2/2 \tag{33}$$

The adaptive law of the weight by means of the chain rule and the gradient descent method can be denoted as:

$$\dot{u}_{kj}^2 = -\tau_1 \frac{\partial P_1}{\partial u_{kj}^2} = -\tau_1 \frac{\partial P_1}{\partial u_2}\frac{\partial u_2}{\partial o_k^3}\frac{\partial o_k^3}{\partial u_{kj}^2} = -\tau_1 \frac{\partial P_1}{\partial u_2} o_j^2 \tag{34}$$

Comparing (32) with (34), yields $\partial P_1/\partial u_2 = -e_r A_e$. Next, the adaptive law of the recurrent weight u_{ik}^1 by means of the chain rule and the gradient descent method can be denoted as:

$$\begin{aligned}\dot{u}_{ik}^1 &= -\eta_2 \frac{\partial P_1}{\partial u_{ik}^1} = -\eta_2 \frac{\partial P_1}{\partial u_2}\frac{\partial u_2}{\partial o_k^3}\frac{\partial o_k^3}{\partial o_j^2}\frac{\partial o_j^2}{\partial o_i^1}\frac{\partial o_i^1}{\partial u_{ik}^1} \\ &= \tau_2 e_r A_e u_{kj}^2 H_j(\cdot) a_i^1(N) O_k^3(N-1)\end{aligned} \tag{35}$$

where τ_2 is the learning rate. To improve convergence and to obtain two optimal learning rates of the weights in the RRHPNN, mend ACO is presented in the following explanation.

A basic ACO algorithm [17]-[22] has a significant impact on performance of an algorithm with respect to the two parameters, the probabilistic choice of the solution and the pheromone updated values. The pheromone updated values are affected by two factors, the evaporation rate and the length of the best tour. A set of M ants is randomly distributed over the vertices. Initially, the partial solutions p^s are empty and the pheromone and heuristic variables are set to some initial value. In each iteration, each ant decides based on a probability distribution, which vertex to add to p^s next. The known rule of the probabilistic choice of a solution [17], [18] is typically defined as:

$$p(c_{ij}\,|\,p^s) = \frac{(\tau_{ij})^{\alpha_1}(\eta_{ij})^{\beta_1}}{\left[\sum_{c_{il}\in M(p^s)} (\tau_{il})^{\alpha_1}(\eta_{il})^{\beta_1}\right]} \quad \forall c_{ij} \in M(p^s) \tag{36}$$

where $M(p^s)$ is the feasible neighborhood given the current partial solution p^s. In addition, τ_{ij} and η_{ij} are the pheromone value and the heuristic value associated with the component c_{ij}, respectively. α_1 and β_1 are positive real parameters whose values determine the relative importance of the pheromone and heuristic information. By moving from vertex i to vertex j, the ants add the associated solution component c_{ij} to their partial solution p^s until they reach their terminal vertex and complete their candidate solutions. These candidate solutions are evaluated and the resulting values are used to update the pheromone values [17]-[22] by:

$$\tau_{ij} = (1-\varphi_1)\tau_{ij} + \varphi_1 \Delta\tau_{best,ij} \tag{37}$$

where $\varphi_1 \in (0,1]$ is the evaporation rate. $\Delta\tau_{best,ij} = 1/L_{best}$ if the best ant used edge (i,j) during its tour, while $\Delta\tau_{best,ij} = 0$ if the best ant does not. The pheromone values are a measure of how desirable it is to add the associated solution component to the partial solution. In order to incorporate forgetting, the pheromone values decrease by some factor in each iteration. In this way, the algorithm avoids prematurely converging to suboptimal solutions. In the next iteration, each ant repeats the previous steps. However, the pheromone values are updated and can be used to make better decisions about which vertex to move to. After some stopping criterion has been reached, the values of τ_{ij} and η_{ij} on the graph encode the solution, as they determine by (36) the path with the highest probability of being constructed step-wise from any initial vertex to the final vertex.

There exist various rules to construct $\Delta\tau_{best,ij} = 1/L_{best}$. Of these, the most standard one is to use all of the candidate solutions found in the trial. This update rule is called the ant system (AS) update rule. The method described in this paper uses the AS update rule [17]-[22] due to its easy implementation. In order to improve these methods, the mend ACO algorithm works as follows. In each state, the ants have to determine which action to choose from. It is not known which state this action will take the ants to, since there is generally a set of next states to which the ants can move, according to some probability distribution. At each trial, the ants are initialized randomly over the set of states. The ants add the state-action pair to their constructed partial solutions. No heuristic values are associated with the vertices, since

there is no a priori information available about the quality of the solution components. This is implemented by setting all of the heuristic values to one. It can be seen that η_{ij} disappears from (36) in this case. Since the values of α_1 and β_1 tune the relative importance of the pheromones τ_{ij} and the heuristics η_{ij}, these are also eliminated. The probability of ant *k* being in state *i* taking action *j* is now:

$$p_{m,k}(c_{ij}\left|p^s\right.)=\frac{(\tau_{m,ij})}{\sum_{l\in U_i(p^s)}(\tau_{m,il})},\ m=1,2,\quad \forall c_{ij}\in U_i(p^s) \tag{38}$$

with $U_i(p^s)$ as the action set the ant has at its disposal in state *i*. Thus, the choice of the next action only depends on the value of the pheromone $\tau_{m,ij}, m=1,2$ associated with this vertex. Note that (38) contains no constants that need tuning, making this algorithm much more straightforward to implement than the original ACO algorithm based on (36). The pheromones are initialized equally for all of the vertices and set to a small non-zero value. In every trial, all of the ants construct their solutions until they either have reached the goal state, or the trial exceeds a certain pre-specified limit. The pheromones are then updated according to the following rule:

$$\tau_{m,ij}(N+1)=(1-\varphi_m)\tau_{m,ij}(N)+\varphi_m\sum_{k=1}^{M}\Delta\tau_{m,k,best,ij},\ m=1,2,\ \forall c_{ij}\in M(p^s)\in S_{iter} \tag{39}$$

where $\varphi_m\in(0,1], m=1,2$ is the evaporation rate for the learning rate $\tau_m, m=1,2$. S_{iter} is the set of all the candidate solutions found in the trial. This type of update rule is comparable to the AS update rule. The value of $\Delta\tau_{m,k,best,ij}, m=1,2$ reflects the amount of pheromone ant *k* deposits on the vertices it has visited. This value is defined as follows:

$$\Delta\tau_{m,k,best,ij}=\frac{1}{\sqrt{[t_{m,k}-(1-d_m)]d_m}}-\frac{1}{\sqrt{[t_{m,\max}-(1-d_m)]d_m}},\ m=1,2 \tag{40}$$

where $t_{m,k}, m=1,2$ is the number of steps at ant *k* needed to reach the goal state, $d_m, m=1,2$ is the sample time, which is used to express time in seconds, and $t_{m,\max}, m=1,2$ is the maximum number of steps allowed in a trial. The value of $(1-d_m), m=1,2$ is used to make the amount of pheromone deposit approximately equal to $1/d_m, m=1,2$ when the ant reaches the goal in just one step. The second term in (40) makes sure that the pheromones are not updated when the trial is stopped at the maximum number of time steps and the ant has not yet reached the goal. It is clear that the fitness function, the total amount of pheromones deposited, is maximized if all of the ants find the shortest path.

In summary, the online tuning algorithm of the RRHPNN control is based on two adaptive laws (34) and (35) for the connective weight adjustment and the recurrent weights adjustment with the two optimal learning rates in (38), (39) and (40), respectively. Moreover, the RRHPNN weight appraised errors are fundamentally bounded [35]. The RRHPNN weight appraised errors are bounded to ensure that the control signal is bounded.

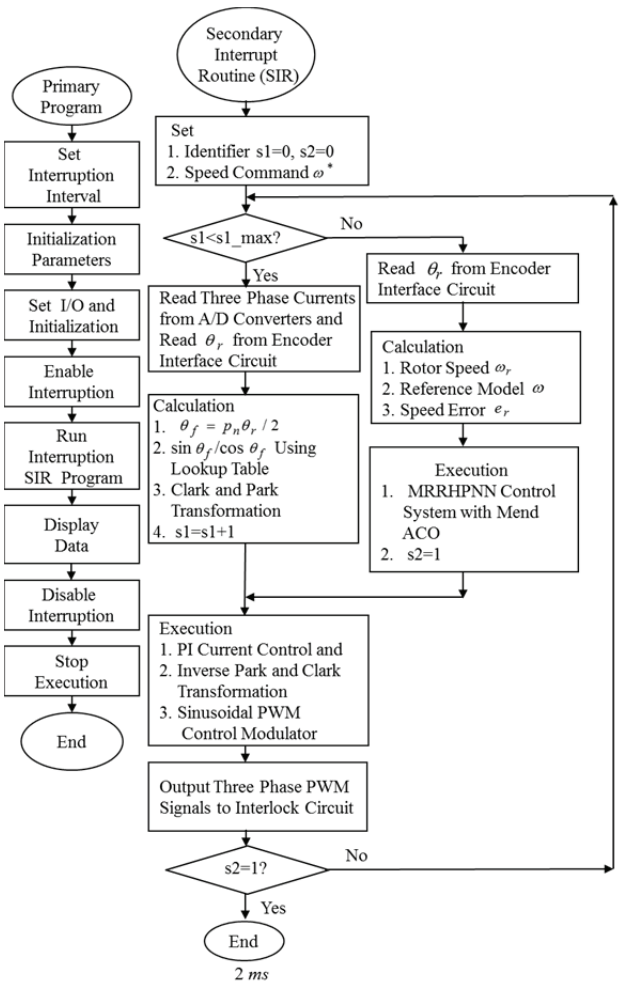

Fig. 5. Flowchart of the executing program by means of a mix signal FPGA system and a DSP control system.

IV. Experimental Results

The entire construction of a SynRM servo-drive CVT system is shown in Fig. 2 by means of a mixed signal FPGA system and a DSP control system. A flowchart of the executed control methodologies with real-time implementation by means of the mixed signal FPGA system and DSP control system consisting of a primary program and a secondary interrupt routine is shown in Fig. 5.

In the primary program, the input/output (I/O) and parameter initializations are processed. Then the interrupt interval for the secondary interrupt routine (SIR) is set. After enabling the interrupt, the main program is used to monitor the control data. A SIR with a 2 *ms* sampling interval is used for reading the rotor position of the SynRM servo-drive CVT system from the encoder interface and the three-phase currents from the analog-to-digital (A/D) converter, calculating the rotor

position and speed, executing the lookup table and coordinate transformation, executing the PI current control, executing the sinusoidal PWM control modulator, executing the MRRHPNN control system with mend ACO, and outputting three-phase PWM signals to the interlock and isolated circuits for switching the three-sets of IGBT power module inverters. The voltage source inverter (VSI) with three-sets of IGBT power modules is switched by current-controlled sinusoidal PWM signals with a switching frequency of 15 *kHz*. To avoid burning the IGBT module for the SynRM servo-drive CVT system at high speed perturbations the SynRM only runs under 3600 *rpm* (376.8 *rad/s*).

Some experimental results are offered to demonstrate the control performance of the proposed MRRHPNN control system with mend ACO. The first is the 1800 *rpm* (188.4 *rad/s*) obtained under the combined parameter variation and the combined unknown nonlinear load torque $T_1^l = \Delta T + T_u$. The second is the 3600 *rpm* (376.8 *rad/s*) obtained under twice the combined parameter variation and the combined unknown nonlinear load torque $T_1^l = 2\Delta T + T_u$. The third is the 3600 *rpm* (376.8 *rad/s*) obtained while adding load under twice the fixed load torque and the combined unknown nonlinear load torque $T_1^l = 2Nm(T_a) + T_u$. All of the gains of the well-known PI controller via inspired knowledge [26-28] are $k_{is} = k_{ps} / T_{is} = 20.6$, $k_{ps} = 9.23$ at 1800 *rpm* (188.4 *rad/s*) under the combined parameter variation and the combined unknown nonlinear load torque $T_1^l = \Delta T + T_u$ for speed tracked to achieve good transient and steady-state control performance. In addition, for a comparison of the control performance with the proposed MRRHPNN control system with mend ACO, the adopted feedforward neural network (FNN) control system with the sigmoid activation function has 2-3-1 neurons in the input-hidden-output layers. Moreover, the two connective weights in the FNN are initialized with random numbers. The control gains of the FNN control are chosen to achieve the better control performance. Further, the control gains of the proposed MRRHPNN control system with mend ACO, which are chosen to achieve the best transient control performance in experimentation considering the requirements of stability, are $\alpha = 0.22$ and $\varepsilon = 0.12$. The adopted RRHPNN has 2-3-1 neurons in the input-hidden-output layers.

Some experimental results of the well-known PI controller for a SynRM servo-drive CVT system at 1800 *rpm* (188.4 *rad/s*) under the combined parameter variation and the combined unknown nonlinear load torque $T_1^l = \Delta T + T_u$, and at 3600 *rpm* (376.8 *rad/s*) under twice the combined parameter variation and the combined unknown nonlinear load torque $T_1^l = 2\Delta T + T_u$ are illustrated in Fig. 6 and Fig. 7, respectively. The responses of the command electromagnetic torque T_e are illustrated in Fig. 6(a) and Fig. 7(a). The speed responses of the command speed ω^*, desired command speed ω, and measured speed ω_r are illustrated in Fig. 6(b) and Fig. 7(b). The responses of a part of the speed error e_r

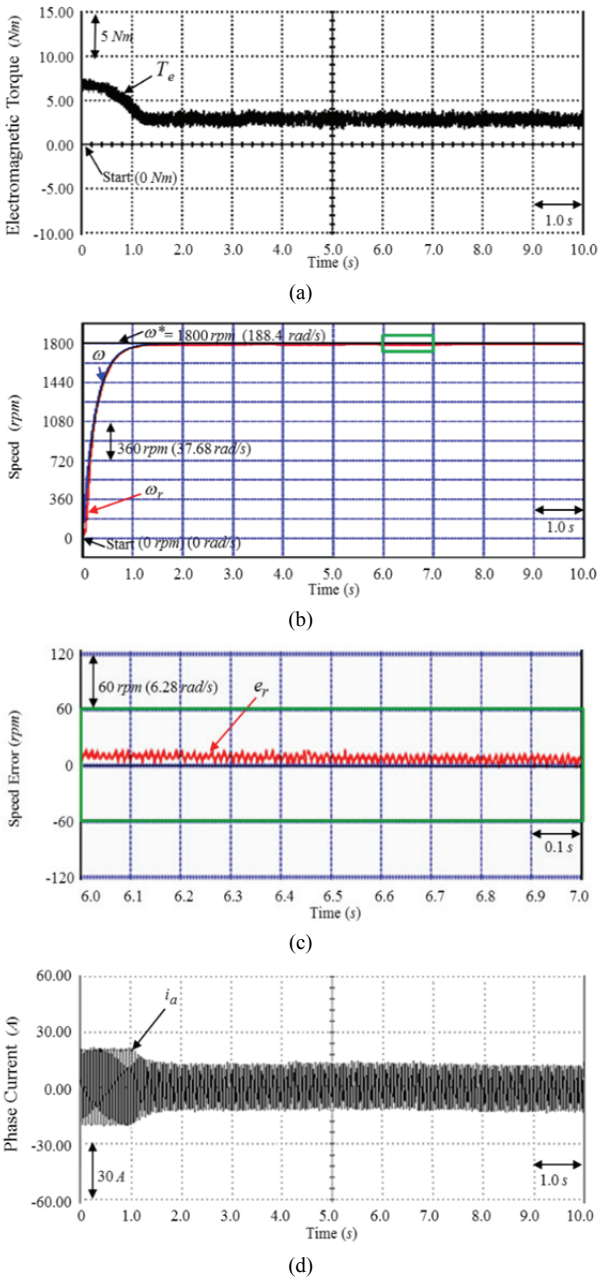

Fig. 6. Tentative results for a SynRM servo-drive CVT system obtained using the well-known PI controller at 1800 *rpm* (188.4 *rad/s*) under the combined parameter variation and the combined unknown nonlinear load torque $T_1^l = \Delta T + T_u$: (a) Response of the electromagnetic torque T_e, (b) Speed response of the command speed ω^*, desired command speed ω, and measured speed ω_r, (c) Response of a part of the speed error e_r, (d) Response of the measured phase current i_a in phase *a*.

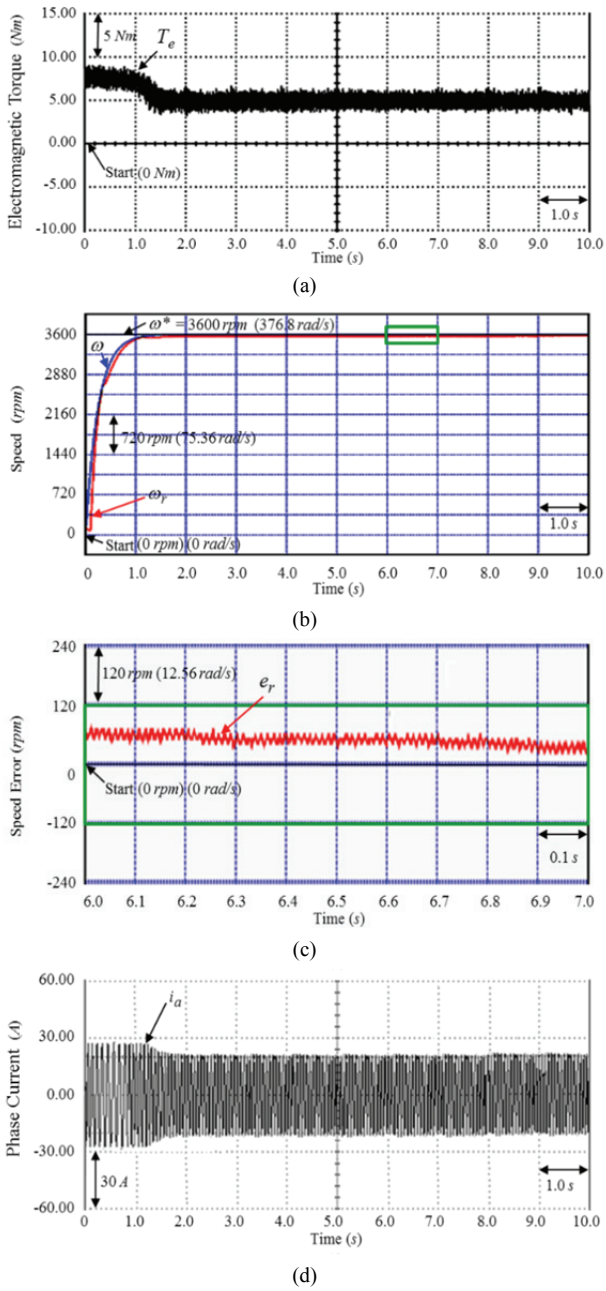

Fig. 7. Experimental results for a SynRM servo-drive CVT system obtained using the well-known PI controller at 3600 *rpm* (376.8 *rad/s*) under twice the combined parameter variation and the combined unknown nonlinear load torque $T_1^l = 2\Delta T + T_u$: (a) Response of the electromagnetic torque T_e, (b) Speed response of the command speed ω^*, desired command speed ω, and measured speed ω_r, (c) Response of a part of the speed error e_r, (d) Response of the measured phase current i_a in phase *a*.

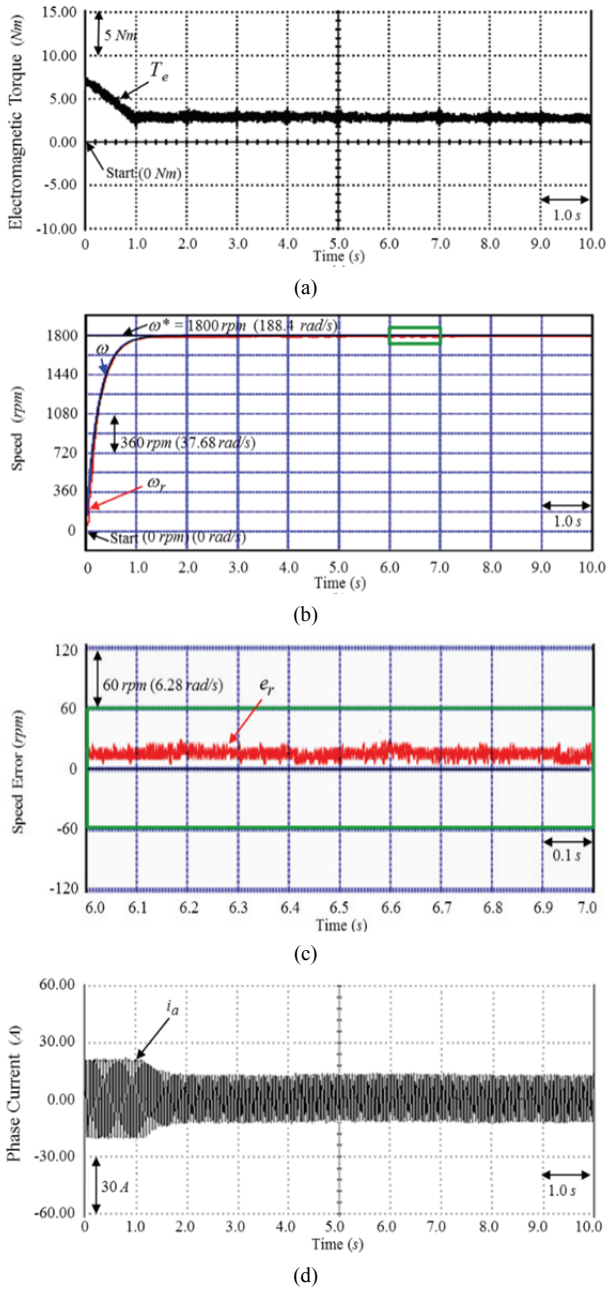

Fig. 8. Experimental results for a SynRM servo-drive CVT system obtained using the three-layer FNN control system at 1800 *rpm* (188.4 *rad/s*) under the combined parameter variation and the combined unknown nonlinear load torque $T_1^l = \Delta T + T_u$: (a) Response of the electromagnetic torque T_e, (b) Speed response of the command speed ω^*, desired command speed ω, and measured speed ω_r, (c) Response of a part of the speed error e_r, (d) Response of the measured phase current i_a in phase *a*.

are illustrated in Fig. 6(c) and Fig. 7(c). The responses of the measured phase current i_a in phase *a* are illustrated by Fig. 6(d) and Fig. 7(d).

The dynamic responses of the command electromagnetic torque T_e shown in Fig. 6(a) and Fig. 7(a) bring about a great torque ripple due to the nonlinear disturbance of the CVT system such as V-belt shaking friction, and action friction between the front pulley and the rear pulley. Low speed operation with a smaller disturbance is the same as that with the nominal case, i.e., $T_e \cong T_1^l$. The speed response

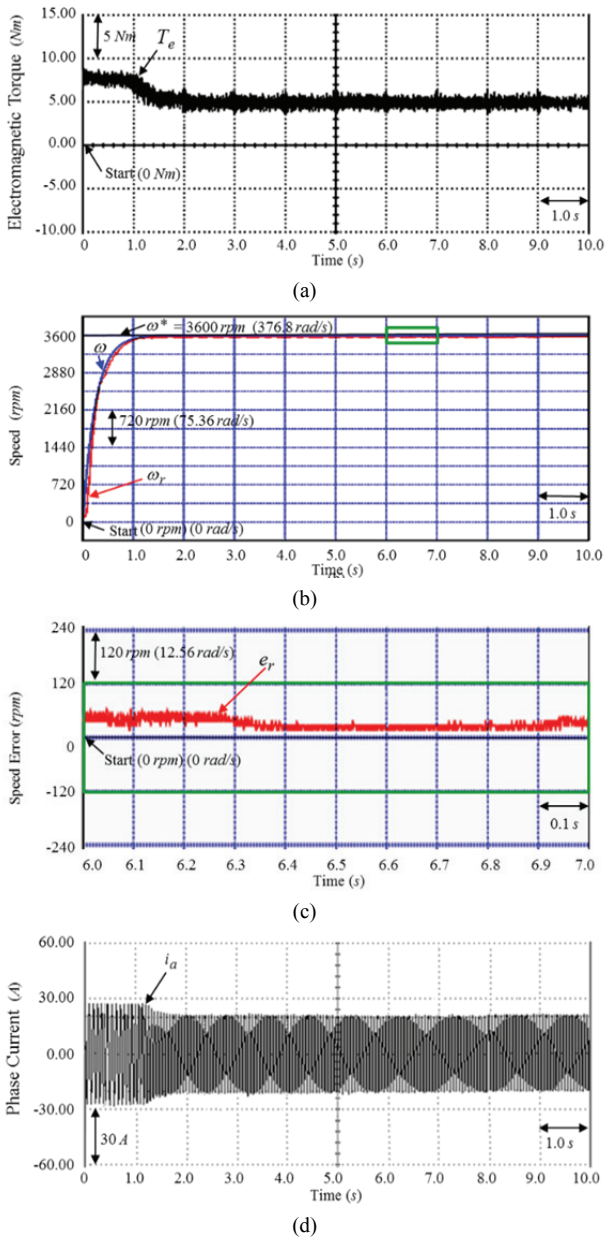

Fig. 9. Experimental results for a SynRM servo-drive CVT system obtained using the three-layer FNN control system at 3600 *rpm* (376.8 *rad/s*) under twice the combined parameter variation and the combined unknown nonlinear load torque $T_1^l = 2\Delta T + T_u$: (a) Response of the electromagnetic torque T_e, (b) Speed response of the command speed ω^*, desired command speed ω, and measured speed ω_r, (c) Response of a part of the speed error e_r, (d) Response of the measured phase current i_a in phase *a*.

with a better tracking performance is illustrated in Fig. 6(b). Moreover, the degenerate tracking response of the speed is illustrated in Fig. 7(b) due to bigger nonlinear disturbances under high speed operation.

Some experimental results obtained with the three-layer FNN control for the SynRM servo-drive CVT system at 1800 *rpm* (188.4 *rad/s*) under the combined parameter variation and the combined unknown nonlinear load torque $T_1^l = \Delta T + T_u$, and at 3600 *rpm* (376.8 *rad/s*) under twice the combined parameter variation and the combined unknown nonlinear load torque $T_1^l = 2\Delta T + T_u$ are illustrated in Fig. 8 and Fig. 9, respectively.

The responses of the command electromagnetic torque T_e are illustrated by Fig. 8(a) and Fig. 9(a). The speed responses of the command speed ω^*, desired command speed ω, and measured speed ω_r are illustrated in Fig. 8(b) and Fig. 9(b). The responses of a part of the speed error e_r are illustrated in Fig. 8(c) and Fig. 9(c). The responses of the measured phase current i_a in phase *a* are illustrated in Fig. 8(d) and Fig 9(d). The dynamic responses of the command electromagnetic torque T_e illustrated in Fig. 8(a) and Fig. 9(a) bring about great torque ripple due to nonlinear disturbance of the CVT system such as V-belt shaking friction, and action friction between the front pulley and the rear pulley.

The sluggish responses of the speed with large errors from the experimental results for a SynRM servo-drive CVT system using the well-known PI controller are illustrated in Fig. 7(c). The linear controller has weak robustness under larger nonlinear disturbances due to a lack of appropriate gains tuning or no degenerate nonlinear effect. The speed response with better tracking performance is illustrated in Fig. 8(b) since low speed operation with a smaller disturbance is the same as the nominal case, i.e., $T_e \cong T_1^l$. Moreover, the degenerate tracking response of the speed is illustrated in Fig. 9(b) due to larger nonlinear disturbances at high speed operation. The sluggish responses of the speed with a large error from the experimental results for a SynRM servo-drive CVT system using the three-layer FNN control system are illustrated in Fig. 9(c). The three-layer FNN control system has weak robustness under large nonlinear disturbances due to a lack of appropriate gains tuning or no degenerate nonlinear effect. However, due to the online adaptive mechanism of the three-layer FNN control system, accurate tracking responses of the speed can be obtained. These experimental results show that the three-layer FNN control system has better control performance and a lower torque ripple than the well-known PI controller for a SynRM servo-drive CVT system at 1800 *rpm* (188.4 *rad/s*) under the combined parameter variation and the combined unknown nonlinear load torque $T_1^l = \Delta T + T_u$, and at 3600 *rpm* (376.8 *rad/s*) under twice the combined parameter variation and the combined unknown nonlinear load torque $T_1^l = 2\Delta T + T_u$.

Some experimental results of the proposed MRRHPNN control system with mend ACO for a SynRM servo-drive CVT system at 1800 *rpm* (188.4 *rad/s*) under the combined

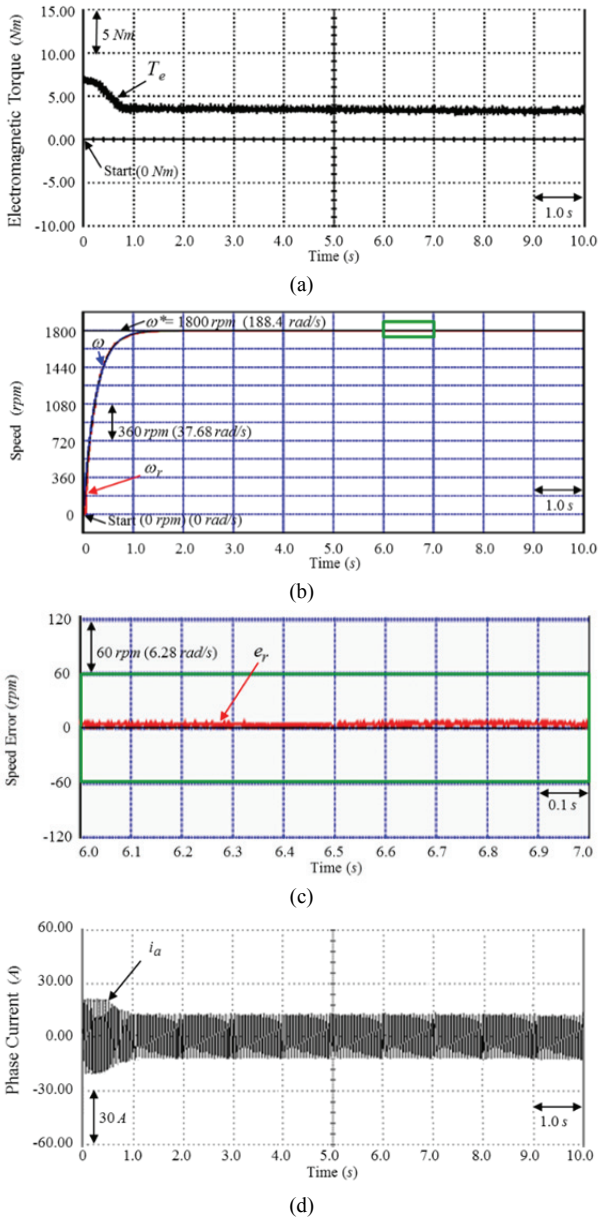

Fig. 10. Experimental results for a SynRM servo-drive CVT system obtained using the MRRHPNN control system with mend ACO at 1800 *rpm* (188.4 *rad/s*) under the combined parameter variation and the combined unknown nonlinear load torque $T_1^l = \Delta T + T_u$: (a) Response of electromagnetic torque T_e, (b) Speed response of the command speed ω^*, desired command speed ω, and measured speed ω_r, (c) Response of a part of the speed error e_r, (d) Response of the measured phase current i_a in phase *a*.

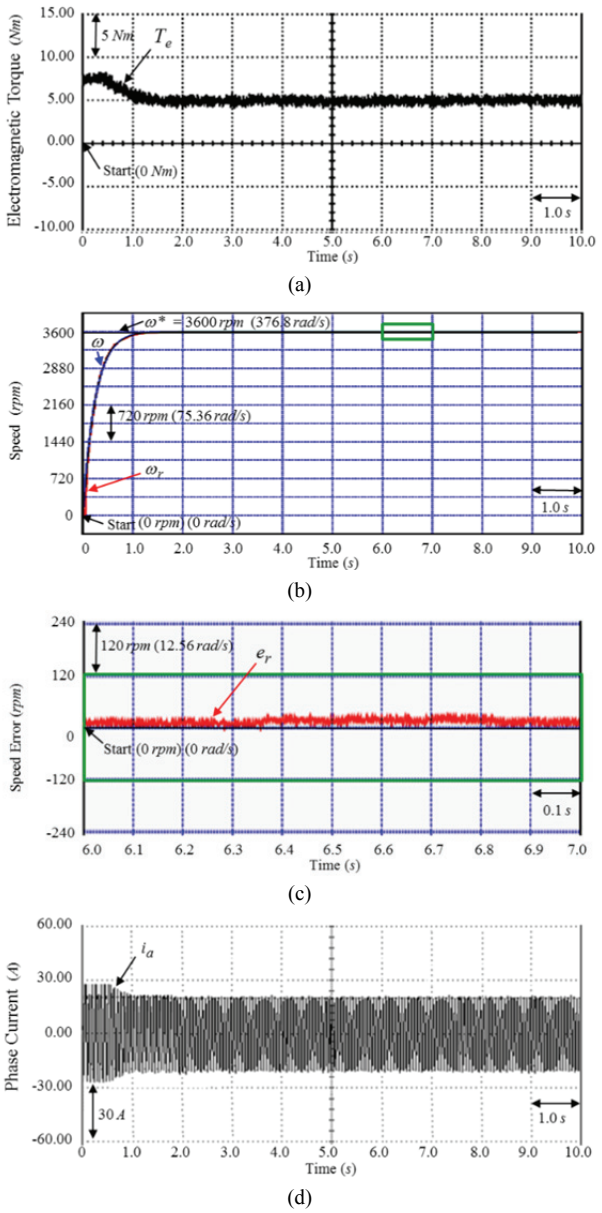

Fig. 11. Experimental results for a SynRM servo-drive CVT system obtained using the MRRHPNN control system with mend ACO at 3600 *rpm* (376.8 *rad/s*) under twice the combined parameter variation and the combined unknown nonlinear load torque $T_1^l = 2\Delta T + T_u$: (a) Response of electromagnetic torque T_e, (b) Speed response of the command speed ω^*, desired command speed ω, and measured speed ω_r, (c) Response of a part of the speed error e_r, (d) Response of the measured phase current i_a in phase *a*.

parameter variation and the combined unknown nonlinear load torque $T_1^l = \Delta T + T_u$, and at 3600 *rpm* (376.8 *rad/s*) under twice the combined parameter variation and the combined unknown nonlinear load torque $T_1^l = 2\Delta T + T_u$ are illustrated in Fig. 10 and Fig. 11, respectively. The responses of the command electromagnetic torque T_e are illustrated in Fig. 10(a) and Fig. 11(a). The speed responses of the command speed ω^*, desired command speed ω, and measured speed ω_r are illustrated in Fig. 10(b) and Fig. 11(b). The responses of a part of the speed error e_r are illustrated in Fig. 10(c) and Fig. 11(c). The responses of the measured phase current i_a in phase *a* are illustrated in Figs. 10(d) and Fig. 11(d). Due to

smaller disturbances, the low-speed operation was the same the nominal case, i.e., $T_e \cong T_1^l$. The speed response shown in Fig. 11(b) demonstrates a higher tracking performance. The experimental results show that accurately tracked performance was achieved for the SynRM servo-drive CVT system when the MRRHPNN control system with mend ACO was used, due to the online adaptive mechanism of the RRHPNN control and the operation of the reimbursed controller. The dynamic response of the command electromagnetic torque T_e brings about a lower torque ripple by the online adjustment of the RRHPNN to cope with the high-frequency unmodeled dynamic of the nonlinear disturbances of the CVT system, such as V-belt shaking friction, and action friction between the front pulley and the rear pulley. Therefore, these experimental results show that the MRRHPNN control system with mend ACO has better control performance than the well-known PI controller and the three-layer FNN control system under high speed perturbations for the SynRM servo-drive CVT system.

Finally, the condition under load torque disturbances and parameter variations $T_1^l = 2\,Nm\,(T_a) + T_u$ with adding a load at the measured rotor speed responses is tested using the well-known PI controller, the three-layer FNN control system and the MRRHPNN control system with mend ACO. The experimental result of the load adjustment when the well-known PI controller, the three-layer FNN control system, and the MRRPHNN with mend ACO were used with adding a load under twice the fixed load torque and the combined unknown nonlinear load torque $T_1^l = 2\,Nm\,(T_a) + T_u$ at 3600 *rpm* (376.8 *rad/s*) are shown in Fig. 12, Fig. 13 and Fig. 14, respectively.

Experimental results of the measured rotor speed response and the measured phase current i_a in phase *a* when the well-known PI controller was used with adding a load under twice the fixed load torque and the combined unknown nonlinear load torque $T_1^l = 2Nm(T_a) + T_u$ at 3600 *rpm* (376.8 *rad/s*) are shown in Fig. 12(a) and Fig. 12(b), respectively. Experimental results of the measured rotor speed response and the measured phase current i_a in phase *a* when the three-layer FNN control system was used with adding a load under twice the fixed load torque and the combined unknown nonlinear load torque $T_1^l = 2Nm(T_a) + T_u$ at 3600 *rpm* (376.8 *rad/s*) are shown in Fig. 13(a) and Fig. 13(b), respectively.

Experimental results of the measured rotor speed response and the measured phase current i_a in phase *a* when the MRRHPNN control system with mend ACO was used with adding a load under twice the fixed load torque and the combined unknown nonlinear load torque $T_1^l = 2Nm(T_a) + T_u$ at 3600 *rpm* (376.8 *rad/s*) are shown in Fig. 14(a) and Fig. 14(b), respectively. These experimental results show that the degenerated responses with adding a load under twice the

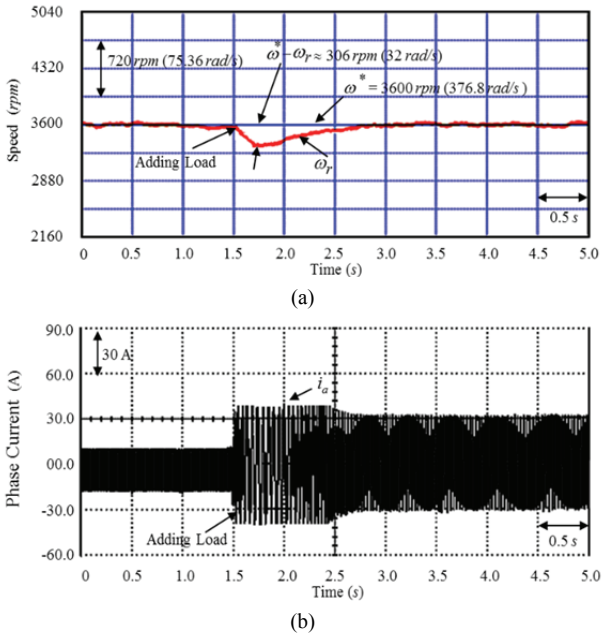

Fig. 12. Experimental results of a SynRM servo-drive CVT system obtained using the well-known PI controller with adding a load under twice the fixed load torque and the combined unknown nonlinear load torque $T_1^l = 2Nm(T_a) + T_u$ at 3600 *rpm* (376.8 *rad/s*): (a) Speed-adjusted response of the command rotor speed ω^* and the measured rotor speed ω_r, (b) Response of the measured phase current i_a in phase *a*.

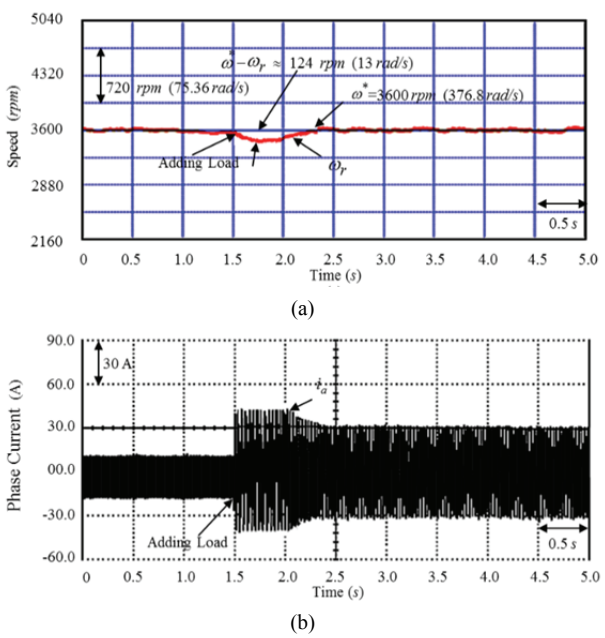

Fig. 13. Experimental results of a SynRM servo-drive CVT system obtained using the three-layer FNN control system with adding a load under twice the fixed load torque and the combined unknown nonlinear load torque $T_1^l = 2Nm(T_a) + T_u$ at 3600 *rpm* (376.8 *rad/s*): (a) Speed-adjusted response of the command rotor speed ω^* and the measured rotor speed ω_r, (b) Response of the measured phase current i_a in phase *a*.

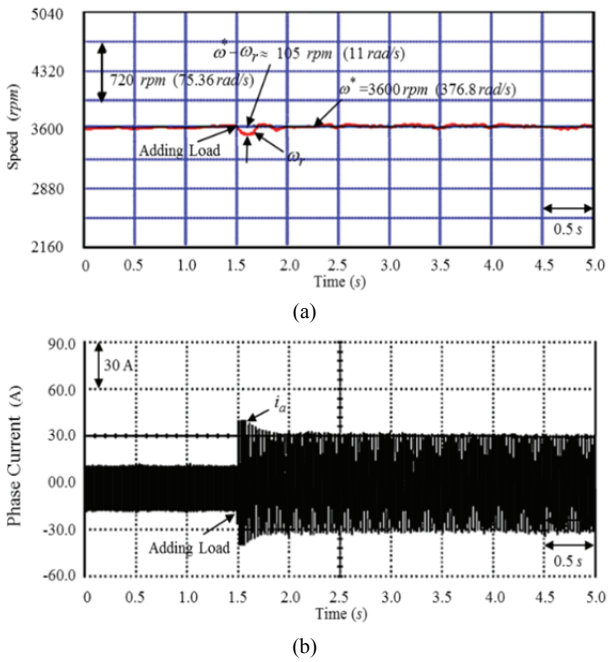

Fig. 14. Experimental results of a SynRM servo-drive CVT system obtained using the MRRHPNN control system with mend ACO with adding a load under twice the fixed load torque and the combined unknown nonlinear load torque $T_1^l = 2Nm(T_a) + T_u$ at 3600 *rpm* (376.8 *rad/s*): (a) Speed-adjusted response of the command rotor speed ω^* and the measured rotor speed ω_r, (b) Response of the measured phase current i_a in phase *a*.

fixed load torque and the combined unknown nonlinear load torque $T_1^l = 2Nm(T_a) + T_u$ are considerably improved when the MRRHPNN control system with mend ACO is used.

Moreover, the transient response of the MRRHPNN control system with mend ACO exhibits a faster convergence and a more favorable load regulation than the well-known PI controller and the three-layer FNN control system.

A comparison of control performance using the three-layer FNN control system, the well-known PI controller and the proposed MRRHPNN control system with mend ACO is presented in Table 1 via three sets of experimental results. The smaller tracked error of the MRRHPNN control system with mend ACO is in evidence. When compared to the three-layer FNN control system and the well-known PI controller, the listed measurements show that the proposed MRRHPNN control system with mend ACO demonstrates the advantageous performance. Moreover, a comparison of the characteristic performances of the well-known PI controller, the three-layer FNN control system and the proposed MRRHPNN control system with mend ACO is presented in Table 2 via three sets of experimental results. According to the four listed performances, the proposed MRRHPNN control system with mend ACO demonstrates better characteristic performance than the three-layer FNN control system and the well-known PI controller.

TABLE I
PERFORMANCE COMPARISON OF THREE CONTROL SYSTEMS

Three Test Cases / Performance	Well-Known PI Controller		
	1800 *rpm* (188.4 *rad/s*) under the combined parameter variation and the combined unknown nonlinear load torque	3600 *rpm* (376.8 *rad/s*) under twice the combined parameter variation and the combined unknown nonlinear load torque	3600 *rpm* (376.8 *rad/s*) with adding load under twice the fixed load torque and the combined unknown nonlinear load torque
T_1^l	$\Delta T + T_u$	$2\Delta T + T_u$	$2Nm(T_a) + T_u$
Max. Error	86 *rpm* (9 *rad/s*)	210 *rpm* (22 *rad/s*)	306 *rpm* (32 *rad/*)
RMS Error	38 *rpm* (4 *rad/s*)	96 *rpm* (10 *rad/s*)	143 *rpm* (15 *rad/s*)
Three Test Cases / Performance	Three-Layer FNN Control System		
	1800 *rpm* (188.4 *rad/s*) under the combined parameter variation and the combined unknown nonlinear load torque	3600 *rpm* (376.8 *rad/s*) under twice the combined parameter variation and the combined unknown nonlinear load torque	3600 *rpm* (376.8 *rad/s*) with adding load under twice the fixed load torque and the combined unknown nonlinear load torque
T_1^l	$\Delta T + T_u$	$2\Delta T + T_u$	$2Nm(T_a) + T_u$
Max. Error	76 *rpm* (8 *rad/s*)	191 *rpm* (20 *rad/s*)	124 *rpm* (13 *rad/s*)
RMS Error	38 *rpm* (4 *rad/s*)	86 *rpm* (9 *rad/s*)	57 *rpm* (6 *rad*/s)
Three Test Cases / Performance	MRRHPNN Control System with Mended ACO		
	1800 *rpm* (188.4 *rad/s*) under the combined parameter variation and the combined unknown nonlinear load torque	3600 *rpm* (376.8 *rad/s*) under twice the combined parameter variation and the combined unknown nonlinear load torque	3600 *rpm* (376.8 *rad/s*) with adding load under twice the fixed load torque and the combined unknown nonlinear load torque
T_1^l	$\Delta T + T_u$	$2\Delta T + T_u$	$2Nm(T_a) + T_u$
Max. Error	67 *rpm* (7 *rad/s*)	172 *rpm* (18 *rad/s*)	105 *rpm* (11 *rad/s*)
RMS Error	29 *rpm* (3 *rad/s*)	67 rpm (7 *rad/s*)	38 *rpm* (4 *rad/s*)

TABLE II
CHARACTERISTIC PERFORMANCE COMPARISON OF THREE CONTROL SYSTEMS

Control System / Characteristic Performance	Well-Known PI Controller	Three-Layer FNN Control System	MRRHPNN Control System with Mended ACO
Dynamic Response	Slow	Fast	Faster
Load Regulation Capability	Poor	Good	Best
Convergence Speed	Low	Middle	High
Two Learning Rates	Not Applicable	Fixed	Variable

V. CONCLUSIONS

A MRRHPNN control system with mend ACO has been successfully applied in controlling a SynRM servo-drive CVT system with robust performance. The MRRHPNN control system with mend ACO can perform overlooker control based on the uncertainty bounds of the controlled

system, and it was designed to stabilize the system states within a predetermined bound area. The main contributions of this study are as follows. (1) Simplified dynamic and kinematic models of a CVT system driven by a SynRM with unknown nonlinear and time-varying characteristics have been successfully derived. (2) The MRRHPNN control system with mend ACO for a SynRM servo-drive CVT system under the occurrence of lumped nonlinear load disturbances was successfully applied to enhance robustness. (3) The adaptive law of online parameter tuning in the RRHPNN and the appraised law of the reimbursed controller were successfully derived using the Lyapunov stability theorem. (4) Two optimal learning rates in terms of connective weights and recurrent weights in the RRHPNN depending on the mend ACO algorithm were successfully used to achieve a faster convergence. (5) The MRRHPNN control system with mend ACO has an improved online learning capability for quickly capturing the nonlinear and time-varying behavior of a system. (6) The proposed MRRHPNN control system with mend ACO has a lower torque ripple than the well-known PI controller and the three-layer FNN control system.

Finally, the control performance of the proposed MRRHPNN control system with mend ACO is better suited to SynRM servo-drive CVT systems when compared with the well-known PI controller and the three-layer FNN control system.

REFERENCES

[1] Y. H. Kim and J. H. Lee, "Optimum design criteria of an ALA-SynRM for the maximum torque density and power factor improvement," *Int. J. Applied Electromagn. Mech.,* Vol. 53, No. S2, pp. S279-S288, 2017.

[2] W. Chai, W. Zhao, and B. Kwon, "Optimal design of wound field synchronous reluctance machines to improve torque by increasing the saliency ratio," *IEEE Trans. Magn.*, Vol. 53, No. 11, Nov. 2017.

[3] R. E. Betz, R. Lagerquist, M. Jovanovic, T. J. E. Miller, and R. H. Middleton, "Control of synchronous reluctance machines," *IEEE Trans. Ind. Appl.*, Vol. 29, No. 6, pp. 1110-1122, Nov./Dec. 1993.

[4] K. Uezato, T. Senjyu, and Y. Tomori, "Modeling and vector control of synchronous reluctance motors including Stator Iron Loss," *IEEE Trans. Ind. Appl.*, Vol. 30, No. 4, pp. 971-976, July/Aug. 1994.

[5] T. Matsuo, A. E. Antably, and T. A. Lipo, "A new control strategy for optimum-efficiency operation of a synchronous reluctance Motor," *IEEE Trans. Ind. Appl.*, Vol. 33, No. 5, pp. 1146-1153, Sep./Oct. 1997.

[6] E. M. Rashad, T. S. Radwan, and M. A. Rahman, "A maximum torque per ampere vector control strategy for synchronous reluctance motors considering saturation and iron losses," *IEEE Industry Applications Conference,* pp. 2411-2417, 2004.

[7] C. Y. Tseng, Y. F. Lue, Y. T. Lin, J. C. Siao, C.H. Tsai, and L. M. Fu, "Dynamic simulation model for hybrid electric scooters," *IEEE Int. Symp. Industrial Electronics*, pp. 1464-1469, 2009.

[8] L. Guzzella and A. M. Schmid, "Feedback linearization of spark-ignitionengines with continuously variable transmissions," *IEEE Trans. Contr. Syst. Technol.,* Vol. 3, No. 1, pp. 54-58, Feb. 1995.

[9] W. Kim and G. Vachtsevanos, "Fuzzy logic ratio control for a CVThydraulic module," *Proc. of the IEEE Symp. Intelligent Control*, pp. 151-156, 2000.

[10] G. Carbone, L. Mangialardi, B. Bonsen, C. Tursi, and P. A. Veenhuizen, "CVT dynamics: Theory and experiments," *Mechanism and Machine Theory*, Vol. 42, No. 4, pp. 409-428, Apr. 2007.

[11] M. N. Eskander, "Minimization of losses in permanent magnet synchronous motors using neural network," *J. Power Electron.,* Vol. 2, No. 3, pp 220-229, Jul. 2002.

[12] A. F. Payam, M. N. Hashemnia and J. Faiz, "Robust DTC control of doubly-fed induction machines based on input-output feedback linearization using recurrent neural networks," *J. Power Electron.,* Vol. 11, No. 5, pp. 719-725, Sep. 2011.

[13] C. H. Lin, "A PMSM driven electric scooter system with V-belt continuously variable transmission using novel hybrid modified recurrent Legendre neural network control," *J. Power Electron.,* Vol. 15, No. 1, pp 220-229, Jan. 2015.

[14] C. H. Lin, "A backstepping control of LSM drive systems using adaptive modified recurrent Laguerre OPNNUO," *J. Power Electron.*, Vol. 16, No. 2, pp. 598-609, Mar. 2016.

[15] C. H. Lin, "Dynamic control of V-belt continuously variable transmission-driven electric scooter using hybrid modified recurrent Legendre neural network control system," *Nonlinear Dynamics*, Vol. 79, No. 2, pp. 787-808, Jan. 2015.

[16] C. H. Lin, "Comparative dynamic control for continuously variable transmission with nonlinear uncertainty using blend amend recurrent Gegenbauer-functional-expansions neural network," *Nonlinear Dynamics*, Vol. 87, No. 3, pp. 1467-1493, Feb. 2017.

[17] M. Dorigo, V. Maniezzo, and A. Colorni, "The ant system: optimization by a colony of cooperating agents," *IEEE Trans. Syst., Man, and Cybernetics-Part B*, Vol. 26, No.1, pp. 29-41, Feb.1996.

[18] M. Dorigo and L. Gambardella, "Ant colony system: A cooperative learning approach to the traveling salesman problem," *IEEE Trans. Evol. Comput.,* Vol. 1, No. 1, pp. 53-66, Apr. 1997.

[19] G. D. Caro and M. Dorigo, "AntNet: A mobile agents approach to adaptive routing," *Technical Report, IRIDIA-Free Brussels University,* Belgium, 1997.

[20] W. J. Gutjahr. "A graph-based ant system and its convergence," *Future Gener. Comput. Syst.*, Vol. 16, No. 8, pp.873-888, Jun. 2000.

[21] M. Dorigo and T. Stützle. *Ant Colony Optimization*, MIT Press, Cambridge, Massachusetts, 2004.

[22] M. Dorigo and C. Blum, "Ant colony optimization theory: A survey," *Theoretical Comput. Sci.*, Vol. 344, No. 2-3, pp. 243-278, Nov. 2005.

[23] R. Gan, Q. Guo, H. Chang, and Y. Yi, "Improved ant colony optimization algorithm for the traveling salesman

problems," *J. Syst. Eng. Electron.*, Vol. 21, No. 2, pp. 329-333, April 2010.
[24] J. Yang and Y. Zhuang, "An improved ant colony optimization algorithm for solving a complex combinatorial optimization problem," *Applied Soft Comput.,* Vol. 10, No. 2, pp. 653-660, Mar. 2010.
[25] H. Idris, A. E. Ezugwu, S. B. Junaidu, and A. O. Adewumi, "An improved ant colony optimization algorithm with fault tolerance for job scheduling in grid computing systems," Plos One, Vol. 12, No. 5, e0177567, 2017.
[26] K. J. Astrom and T. Hagglund, *PID Controller: Theory, Design, and Tuning*, Instrument Society of America, Research Triangle Park, North Carolina, USA, 1995.
[27] T. Hagglund and K. J. Astrom, "Revisiting the Ziegler-Nichols tuning rules for PI control," *Asian J. Contr.*, Vol. 4, No. 4, pp. 364-380, 2002.
[28] T. Hagglund and K. J. Astrom, "Revisiting the Ziegler-Nichols tuning rules for PI control-part II: the frequency response method," *Asian J. Contr.*, Vol. 6, No. 4, pp. 469-482, 2004.
[29] L. Ma and K. Khorasani, "Constructive feedforward neural networks using Hermite polynomial activation functions," *IEEE Trans. Neural Netw.,* Vol. 16, No. 4, pp. 821-833, Jul. 2005.
[30] L. Ma and K. Khorasani, "Adaptive constructive neural networks using Hermite polynomials for image compression," *2nd International Symposium on Neural Networks*, pp. 713-722, 2005.
[31] G. G. Rigatos and S. G. Tzafestas, "Feed-forward neural networks using Hermite polynomial activation functions," *4th Helenic Conference on Advances in Artificial Intelligence, SETN 2006,* pp. 323-333, 2006.
[32] S. M. Siniscalchi, J. Li, and C. H. Lee, "Hermitian polynomial for speaker adaptation of connectionist speech recognition systems," *IEEE Trans. Audio, Speech, Language Process.*, Vol. 21, No. 10, pp. 2152-2161, Oct. 2013.
[33] J. J. E. Slotine and W. Li, *Applied Nonlinear Control*, Englewood Cliffs, Prentice-Hall, New Jersay, 1991.
[34] K. J. Astrom and B. Wittenmark, *Adaptive Control*, Addison-Wesley, New York, 1995.
[35] F. L. Lewis, J. Campos, and R. Selmic, *Neuro-Fuzzy Control of Industrial Systems with Actuator Nonlinearities.* SIAM Frontiers in Applied Mathematics, 2002.

Jung-Chu Ting was born in Pingtung, Taiwan. He received his M.S. degree from Dayeh University, Changhua, Taiwan, in 2004. He became a Ph.D. candidate at the National Changhua University, Changhua, Taiwan, in 2017. His current research interests include power electronics, applications of control theory, and motor control.

Der-Fa Chen was born in Taipei, Taiwan. He received his M.S. degree from the National Chiao Tung University, Hsinchu, Taiwan, in 1988; and his Ph.D. degree from the National Taiwan University of Science and Technology, Taipei, Taiwan, in 2000. From February 2003 to July 2006, he was an Associate Professor in the Department of Industrial Education and Technology, National Changhua University of Education, Changhua, Taiwan, where he has been working as a Professor since August 2006. His current research interests include power electronics, applications of control theory, and motor control.